RESEARCH ARTICLE

Key Points:
- The first P-to-S receiver function study of mantle discontinuities beneath the Malawi and Luangwa rifts with unprecedented spatial coverage
- Normal MTZ thicknesses beneath most areas, precluding thermal upwelling as the dominant rifting mechanism
- The central Malawi rift is developing in a thick and strong lithosphere, leading to a wide rifted basin due to strain delocalization

Supporting Information:
- Supporting Information S1

Correspondence to:
S. S. Gao,
sgao@mst.edu

Passive rifting of thick lithosphere in the southern East African Rift: Evidence from mantle transition zone discontinuity topography

Cory A. Reed[1], Kelly H. Liu[1], Patrick R. N. Chindandali[2], Belarmino Massingue[3], Hassan Mdala[2], Daniel Mutamina[4], Youqiang Yu[1,5], and Stephen S. Gao[1]

[1]Geology and Geophysics Program, Missouri University of Science and Technology, Rolla, Missouri, USA, [2]Geological Survey Department, Zomba, Malawi, [3]Departamento de Geologia, Universidade Eduardo Mondlane, Maputo, Mozambique, [4]Geological Survey Department, Lusaka, Zambia, [5]State Key Laboratory of Marine Geology, Tongji University, Shanghai, China

Abstract To investigate the mechanisms for the initiation and early-stage evolution of the nonvolcanic southernmost segments of the East African Rift System (EARS), we installed and operated 35 broadband seismic stations across the Malawi and Luangwa rift zones over a 2 year period from mid-2012 to mid-2014. Stacking of over 1900 high-quality receiver functions provides the first regional-scale image of the 410 and 660 km seismic discontinuities bounding the mantle transition zone (MTZ) within the vicinity of the rift zones. When a 1-D standard Earth model is used for time-depth conversion, a normal MTZ thickness of 250 km is found beneath most of the study area. In addition, the apparent depths of both discontinuities are shallower than normal with a maximum apparent uplift of 20 km, suggesting widespread upper mantle high-velocity anomalies. These findings suggest that it is unlikely for a low-velocity province to reside within the upper mantle or MTZ beneath the nonvolcanic southern EARS. They also support the existence of relatively thick and strong lithosphere corresponding to the widest section of the Malawi rift zone, an observation that is consistent with strain localization models and fault polarity and geometry observations. We postulate that the Malawi rift is driven primarily by passive extension within the lithosphere attributed to the divergent rotation of the Rovuma microplate relative to the Nubian plate, and that contributions of thermal upwelling from the lower mantle are insignificant in the initiation and early-stage development of rift zones in southern Africa.

1. Introduction

The East African Rift System represents various stages of continental rifting, from the magmatic rift propagators of the Afar Depression currently transitioning toward incipient seafloor spreading [*Bastow et al.*, 2011; *Bridges et al.*, 2012; *Reed et al.*, 2014] to the incipient amagmatic Okavango rift zone of Botswana [*Leseane et al.*, 2015; *Yu et al.*, 2015a] (Figure 1a) and thus is an ideal tectonic feature for investigating rifting mechanisms. Seismicity patterns as well as kinematic GPS residual velocity analysis [*Saria et al.*, 2014] clearly delineate the rift segments of the eastern and western branches of the EARS, which divide the African lithosphere into the Nubian and Somalian plates and the Victoria and Rovuma microplates (Figure 1a). The Malawi rift zone (MRZ) constitutes the southernmost segment of the western branch separating the Nubian plate and the Rovuma microplate (Figure 1b), having initiated no earlier than ~8.6 Ma with the onset of volcanics within the Rungwe Volcanic Province in the vicinity of the Nubia-Rovuma-Victoria Triple Junction [*Ebinger et al.*, 1989; *Delvaux et al.*, 1992]. The MRZ, which is nonvolcanic except for its northern tip, demonstrates a succession of alternating polarity half grabens which display along-strike variations of maturity [*Ebinger et al.*, 1987; *Laó-Dávila et al.*, 2015] and potentially propagates southward into Mozambique via the Urema Graben [e.g., *Fonseca et al.*, 2014]. The Luangwa rift zone (LRZ) of Zambia, in contrast, represents the initial continuation of the EARS into the southwestern branch and is a Permo-Triassic rift basin which is potentially being reactivated by the current stress regime [*Banks et al.*, 1995]. The area of the current study is sutured together by a number of Proterozoic Pan-African mobile belts, within which the Malawi and Luangwa rift zones reside [*Fritz et al.*, 2013].

Through the application of a variety of seismic tomography [*Ritsema et al.*, 1999; *Mulibo and Nyblade*, 2013b], geodynamic and waveform modeling [*Ni et al.*, 2005; *Simmons et al.*, 2007], and seismic receiver function
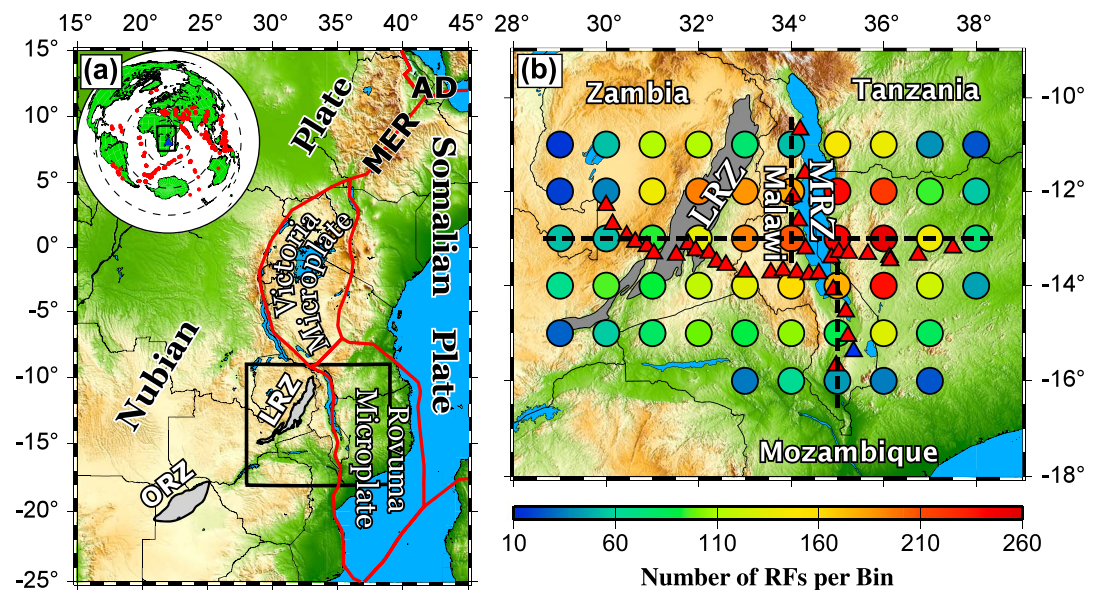
Figure 1. (a) Tectonic basemap of eastern Africa illustrating the EARS plate boundaries (red lines [*Saria et al.*, 2014]). Rectangle encompasses the study area magnified in Figure 1b. AD: Afar Depression; LRZ: Luangwa rift zone; MER: Main Ethiopian Rift; MRZ: Malawi rift zone; ORZ: Okavango rift zone. Inset: Azimuthal equidistant map of the 186 earthquakes employed in this study. (b) Basemap of the Malawi and Luangwa rift zone region depicting the placement of SAFARI (red triangles) seismic stations as well as ZOMB (blue triangle). Colored circles correspond to the number of RFs per 1° radius bin spaced at one geographical degree grouped according to their distribution at ray-piercing points of 535 km depth. Only bins with a minimum RF hit count of 10 are shown. Black dashed lines delineate the E-W and N-S profiles represented in Figures 3a and 3b, respectively.

techniques [*Owens et al.*, 2000; *Huerta et al.*, 2009; *Mulibo and Nyblade*, 2013a], it has been suggested that eastern Africa is underlain by a massive low-velocity structure, probably stretching from the core-mantle boundary to beneath the eastern and western branch rift segments. Shear wave splitting measurements obtained adjacent to the Tanzania Craton, the Main Ethiopian Rift, and the Arabian Peninsula [*Bagley and Nyblade*, 2013] are attributed to mantle flow modulated by northward advection of the African superplume which upwells through the mantle transition zone (MTZ) beneath the northern MRZ. However, shear wave splitting studies conducted throughout north central Africa and Saudi Arabia also demonstrate north-south mantle flow patterns which are attributed to basal traction-generated anisotropy from simple northward plate migration relative to the underlying asthenosphere [*Elsheikh et al.*, 2014; *Lemnifi et al.*, 2015]. Similarly, shear wave splitting evidence from the Okavango rift zone (ORZ, Figure 1a) and southern Africa [*Silver et al.*, 2001; *Yu et al.*, 2015b] indicates that subcrustal mantle anisotropy can be explained by plate motion and lithospheric Archean structures and are not associated with a contemporary flow system related to the proposed African superplume.

One approach often employed to examine the present-day thermal state of the upper mantle and MTZ, and consequently the present-day existence or absence of thermal upwelling through the MTZ, is to study the spatial distribution of the depths to the 410 and 660 km discontinuities (hereafter referred to as the d410 and d660, respectively) [*Ringwood*, 1991]. The d410 and d660 correspond to the phase transition from pyrolitic olivine to wadsleyite (β-spinel) and from ringwoodite (γ-spinel) to perovskite plus magnesiowüstite, respectively [*Ringwood*, 1975]. Impedance contrasts across either discontinuity result in P-to-S converted phases (hereafter referred to as $P410s$ and $P660s$) which render teleseismic analysis especially advantageous with regard to high-resolution mapping of discontinuity structure. Experimental analyses of the phase transitions associated with the discontinuities reveal a positive and negative Clapeyron slope corresponding to the d410 and d660, respectively. Consequently, a high-temperature thermal anomaly in the MTZ would have the effect of thinning the MTZ accomplished by depression of the d410 and uplift of the d660 [*Bina and Helffrich*, 1994] and vice versa for low-temperature environments such as subducting slabs [*Helffrich*, 2000]. The presence of hydrous minerals in the MTZ has the same effects as low temperatures [*Ohtani et al.*, 2004] and may serve to thicken the MTZ through simultaneous uplift and depression of the d410 and d660, respectively [*Litasov et al.*, 2005].

The most recent MTZ study conducted for the central EARS by *Mulibo and Nyblade* [2013a] demonstrates a thinned MTZ beneath the eastern branch as well as to the west of the LRZ in Zambia and the Tanganyika-Rukwa rift system in southwest Tanzania. The authors applied a 3-D velocity model obtained from their earlier work [*Mulibo and Nyblade*, 2013b] to correct for apparent *d*410 and *d*660 depths and interpreted the results as widespread thinning due to the throughgoing African superplume. Receiver function analysis of the MTZ beneath Botswana recently reported by *Yu et al.* [2015a], on the other hand, did not detect a deviation of the MTZ from the global average, thereby providing evidence of the absence of a possible thermal anomaly in the MTZ beneath the ORZ.

Local teleseismic data coverage of the Malawi and Luangwa rifts has heretofore been limited, and as such only low-resolution global [e.g., *French and Romanowicz*, 2015] and African continental-scale [e.g., *Begg et al.*, 2009; *Hansen et al.*, 2012] teleseismic studies have been conducted to investigate crust and mantle velocity structure and discontinuities beneath the southernmost EARS. This study represents the first examination of the MTZ discontinuities beneath the MRZ and LRZ using *P*-to-*S* receiver functions (RFs). We postulate the presence of normal MTZ thicknesses and abnormally thick lithosphere relative to surrounding areas within the vicinity of the southernmost segments of the EARS and argue for passive rift basin development in the absence of active asthenospheric upwelling.

2. Data and Methods

We employ broadband teleseismic data recorded by 35 portable seismic stations that we installed and operated along two profiles in Malawi, Mozambique, and Zambia (Figure 1b) over the period from June 2012 to June 2014. The stations are part of the Seismic Arrays For African Rift Initiation (SAFARI) experiment, which is the passive seismic component of an interdisciplinary project aimed at studying the Okavango, Malawi, and Luangwa rift zones [*Gao et al.*, 2013]. The data set was supplemented by seismic data recorded by AfricaArray station ZOMB, which is the only neighboring station that was operating during the SAFARI deployment. The ~900 km E-W trending array consisting of 26 stations stretches across central Zambia and Malawi into northern Mozambique and bisects the LRZ and MRZ obliquely and orthogonally, respectively, and the ~600 km N-S profile consists of 10 SAFARI stations as well as station ZOMB and parallels the MRZ. Each station was equipped with a Quanterra Q330 digitizer and a Guralp CMG-3T 120 s sensor recording at a continuous rate of 50 Hz. All data utilized in this study are archived with the Incorporated Research Institutions for Seismology (IRIS) Data Management Center (DMC) and are openly accessible starting from mid-2016.

Data are requested for event-station pairs with epicentral distances between 30° and 100° and with variable M_b cutoffs reliant upon epicentral distance and event focal depth in order to maximize data quality [*Liu and Gao*, 2010]. The original Z (vertical), N (north-south), and E (east-west) components are bandpass filtered between 0.02 and 0.2 Hz with a four-pole, two-pass Bessel filter and are rotated into a Z, R (radial), and T (transverse) coordinate system. The resulting radial and vertical components are retained if the signal-to-noise ratio (SNR) on the vertical component exceeds 4.0 (see *Gao and Liu* [2014a] for the specific set of parameters used in evaluating the SNR). The remaining seismograms are first processed using exponential weighting functions to zero out amplitudes in a 10 s window centered on the theoretical arrival of the detrimental *PP* phase, while diminishing weights are applied to the trace at times no earlier and no later than 30 s before and after, respectively, the *PP* arrival. The seismograms are then converted into radial RFs using the procedure of *Ammon* [1991] with a water level of 0.03 and a Gaussian half width of 5 s. A quality control procedure is then applied to remove RFs with high noise or abnormal arrivals. Specifically, RFs with either strong pre-*P* noises or large arrivals in the *P* wave coda are rejected by an automatic cross-correlation procedure. The cutoff SNR and other parameters are the same as those used in *Gao and Liu* [2014b] for imaging the MTZ beneath the contiguous United States. About 10% of the RFs are rejected by this procedure, and a total of 1935 high-quality RFs from 186 events (Figure 1a) are obtained for the study.

Positive-energy arrivals of both the *P*410*s* and *P*660*s* are observed across teleseismic slowness values between 4.5 and 8.5 s per degree for all the RFs (Figures 2b and 2c) and for RFs recorded by stations within the E-W array (Figures 2e and 2f), with either data set demonstrating *d*410 and *d*660 uplifts of approximately 13 km (Figures 2a and 2d) relative to the respective IASP91 depths of 410 and 660 km [*Kennett and Engdahl*, 1991]. RFs recorded along the N-S array (Figures 2h and 2i) demonstrate a weakly positive *d*410 arrival and a stronger *d*660 phase coincident with uplifts of 4 and 11 km, respectively (Figure 2g).
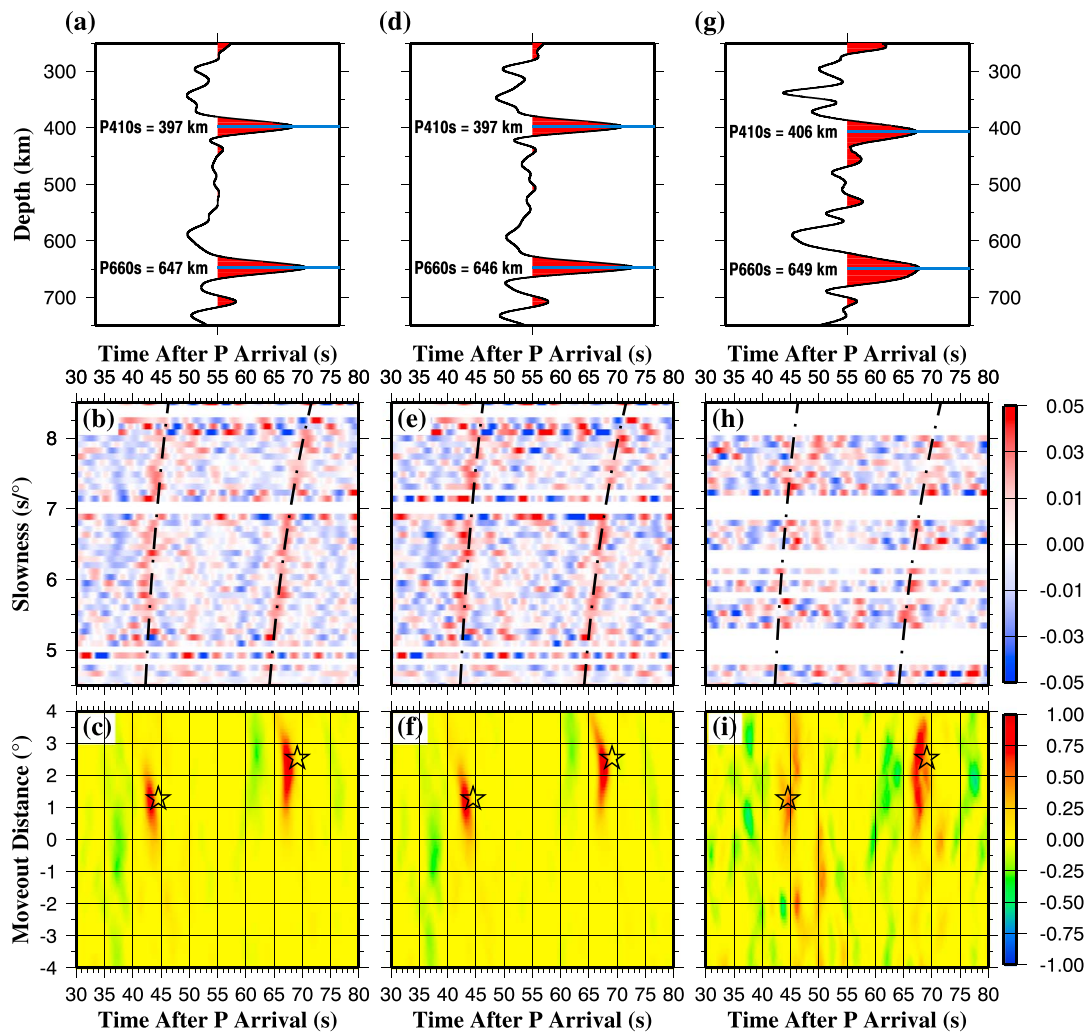
Figure 2. Vespagram analysis panels for (a–c) the entire data set consisting of 1935 RFs, (d–f) the E-W transect of SAFARI stations consisting of 1462 RFs, and (g–i) the N-S SAFARI plus ZOMB array consisting of 527 RFs. (Figures 2a, 2d, and 2g) RF stacks with demonstrated *Ps* phases. (Figures 2b, 2e, and 2h) Slant-stack diagrams of RFs in slowness bins of 0.05 s per degree with a step of 0.05 s per degree with predicted arrival times of the *P410s* and *P660s* according to the IASP91 Earth model (hachured lines). The amplitudes are relative to those of the direct *P* wave. (Figures 2c, 2f, and 2i) Vespagram results for a reference slowness of 6.5 s per degree with stars marking the expected locations of the *P410s* and *P660s*.

We follow the nonplane wave moveout correction and stacking procedure of *Gao and Liu* [2014a] to stack the direct *P*-to-*S* converted phases (*Pds*) within the RFs and to convert the time series RFs into depth series based on the 1-D IASP91 Earth model. While plane wave procedures assume that the direct *P* and the *P*-to-*S* converted phases have the same ray parameter, the nonplane wave procedure takes consideration of the fact that the former has a larger ray parameter than the latter, simply because the conversion point is closer to the station than the piercing point of the direct *P* wave [see *Gao and Liu*, 2014a, Figure 1a]. Depending on the depth of the discontinuity and the ray parameter of the incoming raypath, the plane wave assumption can lead to a bias of several kilometers in the resulting discontinuity depth and, more importantly, a reduction in the stacking amplitude due to incoherent stacking.

RFs with piercing points in radius = 1° circular bins centered on 1° intersecting grid lines of latitude-longitude are stacked using the above procedure to form a depth series for the bin. Note that because the 1-D IASP91 Earth model is used for moveout correction and time-depth conversion, the resulting depths are referred to as apparent rather than true depths. To convert the apparent depths into true depths, reliable Vp and Vs velocity models with a sufficient spatial resolution for the entire upper mantle and MTZ are needed [e.g., *Gao and Liu*, 2014b]. Unfortunately, such models are nonexistent for the study area. Bins with 10 or more RFs are
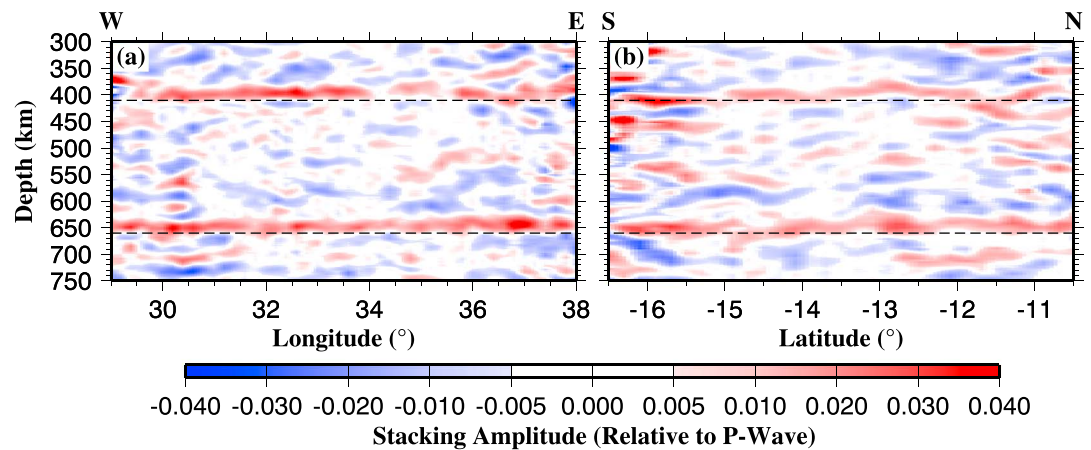
Figure 3. (a) Amplitude profile of 1462 RFs recorded by stations along the E-W transect (Figure 1b) migrated using nonplane wave moveout correction. Dashed lines indicate the IASP91 depths for the d410 and d660. (b) Same as Figure 3a but for the N-S SAFARI plus ZOMB transect consisting of 527 RFs.

plotted in Figure 1b, with a maximum hit count of 255 RFs across the central MRZ. For each bin, 50 bootstrap resamplings [*Efron and Tibshirani*, 1986] of the RFs are used to compute the mean and standard deviation (SD) of the d410 and d660 depths and the resultant MTZ thickness. Subsequently, the P410s and P660s arrivals are manually examined to reject peaks obfuscated by similar-amplitude arrivals or by weak amplitudes. While a larger number of resamplings can improve the accuracy of the resulting mean and SD, the chosen value is the result of considering a balance between accuracy and required computation times, as well as the number of RFs for each of the bins.

To provide a first-order perspective of the MTZ discontinuity spatial distribution, we migrate the RFs along their raypaths for ray-piercing points at depths between 300 and 750 km using nonplane wave moveout traveltimes [*Gao and Liu*, 2014a]. Results shown in Figure 3 display the mean amplitude for grids of 0.2° width and 1 km height, after smoothing using a minimum curvature solution with a tension factor of 0.40 [*Smith and Wessel*, 1990]. The P410s and P660s are clearly observed along both the E-W profile containing 1462 RFs (Figure 3a) and the N-S profile containing 527 RFs (Figure 3b).

3. Results

All of the resulting depth series in the region bounded between 11°S and 16°S and between 29°E and 38°E are represented within the six latitudinal profiles of Figure 4. Additionally, each of the 10 longitudinal profiles are provided in the supporting information (Figure S1), and the resulting d410 and d660 apparent depths and MTZ thicknesses for each of the 54 bins demonstrating a robust P-to-S conversion from either the d410 or the d660 are shown in Table S1. Among the 54 bins, the number of bins with a reliable P410s, P660s, or both phases is 48, 51, and 46, respectively. Nine of the 108 peaks are rejected from MTZ thickness computations due to the low strength and resulting ambiguity in identifying the arrivals corresponding to the MTZ discontinuities (Figure 4).

Examination of the stacked traces sorted according to increasing d410 depth reveals a regional prevalence for parallelism between the discontinuities (Figure 5). Figure 5 also demonstrates that the vast majority of the traces have a d410 and d660 that are apparently shallower than the anticipated values in the IASP91 Earth model. The regional average for either discontinuity is found to be 399.2 ± 6.5 km and 647.9 ± 4.7 km, respectively. While in principle seismic azimuthal anisotropy can lead to azimuthally varying apparent depths by several kilometers, the decent azimuthal coverage of the events (Figure 1a) greatly reduces the influence of anisotropy, and as a consequence the resulting depths reflect the azimuthally averaged values. Additionally, spatial variations of radial anisotropy could also lead to errors in the resulting apparent depths, although the magnitude of the errors cannot be readily evaluated due to a lack of reliable estimates of radial anisotropy for the entire upper mantle and MTZ beneath the study area.
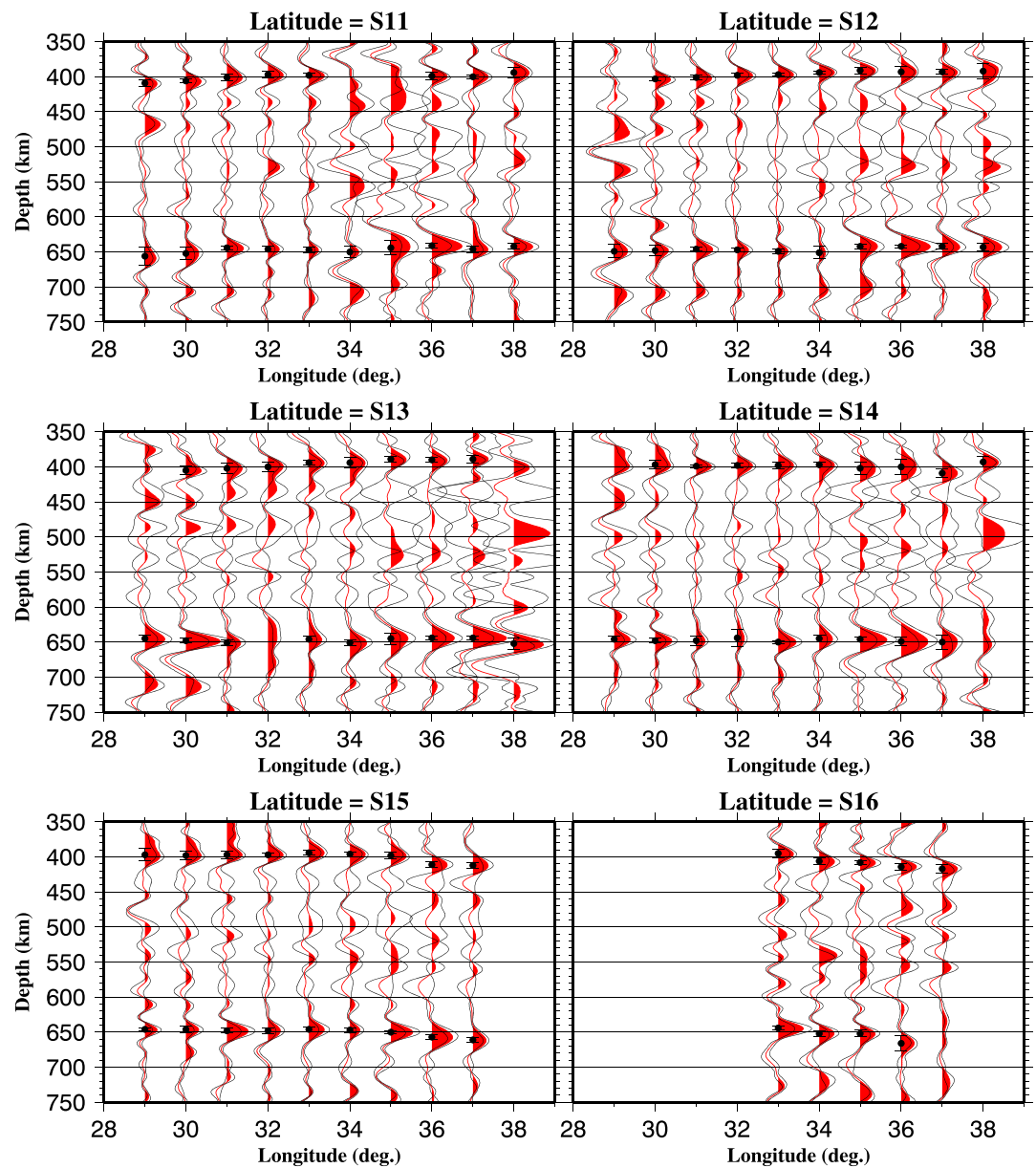
Figure 4. Depth series of stacked RFs in bins of 1° radius along six latitudinal profiles. The red traces demonstrate the mean amplitude averaged over 50 bootstrap iterations, while the thinner black lines indicate the mean amplitude ±2 SD. The black circles delineate the average observed discontinuity depths ±2 SD.

The resulting apparent depths to the $d410$ (Figure 6a) range from roughly 390 km beneath the east central part of the study area in northern Mozambique to a maximum depth of 417 km at the SE corner of the study region. Trends similar to the $d410$ topography are observed for the apparent $d660$ depths (Figure 6b), with minimum depth values of ~640 km beneath the east central part of the study area and 645–650 km beneath the LRZ and northern Zambia. Parallel uplifts of both discontinuities of up to 20 km beneath most of the study area produce a regionally normal MTZ thickness (Figure 6c). Short-wavelength anomalies in the MTZ thickness are observed, including a 6–7 km thickening beneath the central MRZ where we observe the maximum MTZ thicknesses of 256–257 km, a 6–7 km thinning beneath the NW rift flank of the LRZ, and a more localized area of thinner-than-normal MTZ in SW Tanzania (Figure 6c). The MTZ thicknesses are well defined for most of the bins (Figure 6d), with an average standard deviation of 3.8 km for the study area.
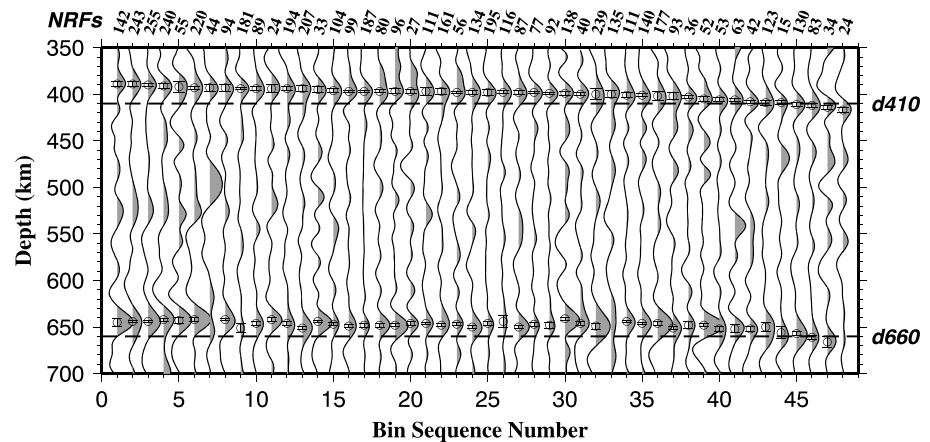
Figure 5. Binned RFs sorted according to increasing apparent depth of the *d*410. The circles and vertical bars on each of the traces represent the mean and 1 SD of the discontinuity depths, and the number on top of each trace indicates the number of RFs used for the stacking.

4. Discussion

The RF analysis procedure employed in this study utilizes the 1-D IASP91 reference Earth model to obtain apparent discontinuity depths. In order to convert these apparent depths into true depths, high-resolution *P* and *S* wave velocity models extending through the upper mantle and MTZ are needed. No such models are available for the study area, and currently available global tomography models are inadequately suited for the requisite high-resolution corrections. In addition, most previous studies show significant variability in MTZ discontinuity depths but not MTZ thickness due to velocity heterogeneities in the upper mantle [e.g., *Gao and Liu*, 2014b; *Thompson et al.*, 2015; *Reed et al.*, 2016]. For the study area, the high correlation between the apparent depths of the *d*410 and *d*660 (Figure 7) similarly suggests that the apparent depth variations are mostly caused by lateral variations of upper mantle velocity anomalies, which affect the apparent depths of both discontinuities approximately equally due to the steep incidence of the *P*-to-*S* converted phases. We therefore infer the nature of the MTZ thermal structure based on the apparent rather than true MTZ discontinuity depths and thicknesses.

4.1. Spatial Variation of Anomalous MTZ Thicknesses

Thirty-five of the 46 bins possessing both a reliable *d*410 and *d*660 provided MTZ thickness estimates within a ±5 km tolerance of the IASP91 250-km global average (Figure 6c). This indicates the regional absence of a thermal anomaly perturbing the MTZ directly beneath either the MRZ or LRZ excepting three distinct areas of note: thinner-than-normal MTZ paralleling the LRZ along the NW flank in NW Zambia, thinner-than-normal MTZ in southern Tanzania, and an area with thicker-than-normal MTZ beneath the central MRZ (Figure 6c).

For the first anomalous region, which is located beneath the NW LRZ flank, tomographic inversions of *P* and *S* relative traveltime residuals measured at AfricaArray stations reveal *P* wave velocity anomalies of −0.5% extending through the upper mantle into the MTZ beneath NW Zambia [*Mulibo and Nyblade*, 2013b]. An MTZ topography study [*Mulibo and Nyblade*, 2013a] employed velocity corrections using the *P* and *S* wave models of *Mulibo and Nyblade* [2013b] to reveal an MTZ thinning as large as 40 km beneath NW Zambia corresponding to a positive temperature anomaly of about 300°C. This is inconsistent with the minor thinning of the MTZ that we observed for the same area. In addition, the low-velocity upper mantle anomalies reported by *Mulibo and Nyblade* [2013b] would lead to an apparent depression of both discontinuities of about 8 km [*Gao and Liu*, 2014a], which is also not observed. In contrast, for NW Zambia, the apparent depths are shallower than normal (Figure 6) and thus suggest higher-than-normal upper mantle velocities. The key piece of information necessary to resolve the inconsistencies between this and previous studies [*Mulibo and Nyblade*, 2013a, 2013b] is a reliable high-resolution determination of both *P* and *S* wave velocities for the entire upper mantle and MTZ. We note that the introduction of a false low-velocity anomaly into the MTZ during velocity corrections can produce an artificial uplift of the resultant *d*660 depth and a thinner-than-real MTZ in order to account for the reduced velocities while maintaining the observed traveltimes. This scenario is discussed quantitatively at length in *Mohamed et al.* [2014].
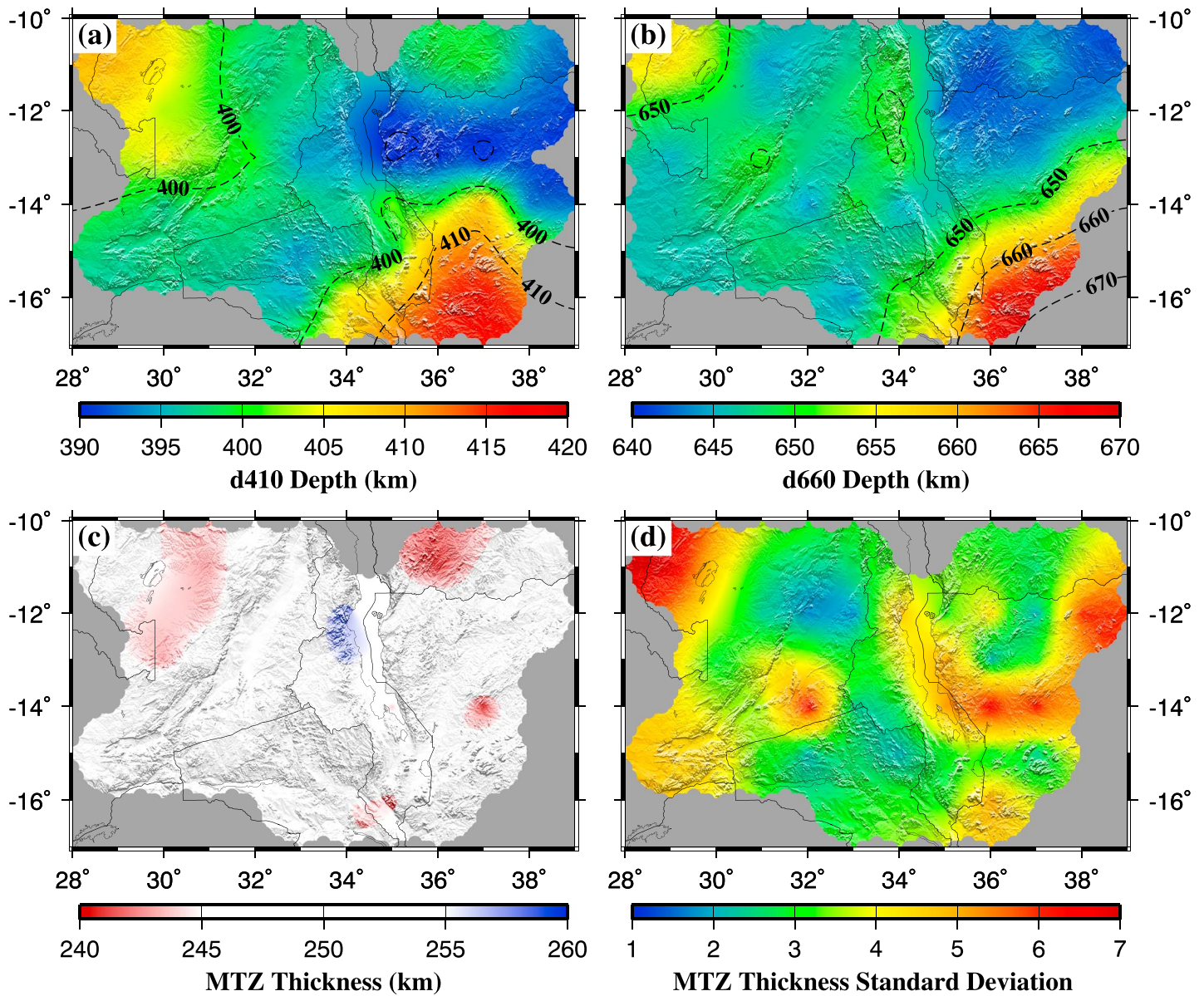
Figure 6. Apparent depths for the (a) *d*410 and (b) *d*660. (c) MTZ apparent thickness results with a tolerance of ±5 km from the IASP91 average of 250 km. (d) SD of the mean MTZ thicknesses. Results are displayed at 0.1° resolution after resampling of available 1° data.

The second anomalous area, which is located in southern Tanzania, is characterized by an MTZ thinning of up to 7 km. It is situated on the edge of the study area and is sampled by a limited number of RFs. If the feature can be confirmed by future studies with additional data, it could indicate ongoing thermal upwelling beneath the area. The third area of anomalous MTZ is located beneath the central MRZ and its western flanking area (Figure 6c). It is characterized by an MTZ which is approximately 8 km thicker than normal. A thicker-than-normal transition zone is most commonly attributed to the passage of lower temperature subducting slabs, to anomalous hydration associated with ongoing or relict slabs, or to the upwelling of lower mantle hydrous features [*Helffrich*, 2000; *Liu et al.*, 2003; *Thompson et al.*, 2015]. Melt atop the *d*410 is associated with the upwelling of hydrous mantle materials [e.g., *Thompson et al.*, 2015], which is unlikely in this area due to the absence of laterally coherent negative-amplitude arrivals atop the *d*410 (Figure 3b). Subduction associated with the current African interior halted with the cessation of Pan-African collision and the closure of Gondwana at ∼500 Ma [*Fritz et al.*, 2013], and thus it is unlikely that negative temperature anomalies are still present in the area. Therefore, the presence of a thicker-than-normal MTZ beneath the
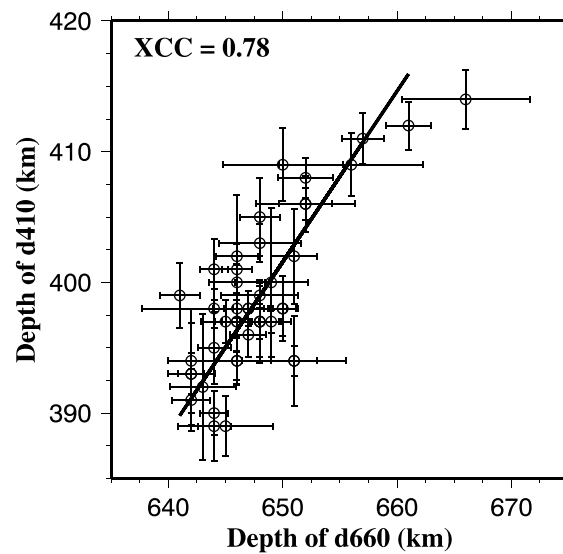
Figure 7. Correlation plot of apparent *d*410 versus *d*660 depth pairs with 1 SD bars. The line indicates the optimal bivariate regression with a cross-correlation coefficient of 0.78.

Malawi rift valley could be related to long-term hydration of the MTZ, probably associated with Proterozoic subduction of Gondwana lithosphere. Recent evidence for enduring hydration within the MTZ subsequent to ancient subducted slab dehydration has been presented through a mantle xenolith and Cenozoic basalt study of NE Asia [*Kuritani et al.*, 2011].

4.2. Rift Development in Thick Lithosphere

The regional parallelism observed between the apparently shallower-than-normal *d*410 and *d*660 (Figures 5 and 7) implies that high-velocity anomalies situated above the *d*410 are responsible for the maximal 20 km uplift of both discontinuities beneath the study area (Figure 6). The most plausible source of an upper mantle high-velocity anomaly beneath the study area, which is devoid of ongoing or recent subduction, is the presence of relatively thick cratonic lithosphere. The existence of thick lithosphere relative to the surrounding area has been revealed by surface wave tomography-generated estimates of lithosphere-asthenosphere boundary (LAB) depths [*Fishwick*, 2010], including a tongue-shaped 180–200 km thick lithosphere across the southern MRZ which may represent the eastward extension of cratonic lithosphere spanning the Congo and Kalahari Cratons. Although the spatial resolution of the surface wave tomography study is not high enough to precisely pinpoint the distribution of the LAB depth, Figure 5 of *Fishwick* [2010] shows that the central southern MRZ has the thickest lithosphere amongst all of the rift segments in the eastern and western branches of the EARS. The presence of a strong lithosphere in the vicinity of the central southern MRZ is also consistent with computations of vertically averaged lithospheric strength conducted by *Stamps et al.* [2014] suggesting that the MRZ is propagating through a region of strong, brittle lithosphere relative to that of the Kenya and Albertine rifts.

This high-velocity corridor is situated in close proximity to a sector of poorly developed border faulting in the central MRZ [*Laó-Dávila et al.*, 2015], which terminates toward the west at the approximate terrane boundary of two Mesoproterozoic Irumide complexes [e.g., *Fritz et al.*, 2013]. It also roughly coincides with a region of anomalously negative isostatic Bouguer gravity values extending beneath the LRZ and eastern Mozambique [*Balmino et al.*, 2012; *Molnar et al.*, 2015], as well as high-velocity anomaly values obtained from surface wave tomography observed across the southern MRZ at depths nearing 200 km [*Fishwick*, 2010]. Remote sensing observations made by *Laó-Dávila et al.* [2015] demonstrate that the central MRZ is characterized by the widest (~75 km) graben geometries within the region of the proposed high-velocity corridor. *Laó-Dávila et al.* [2015] also postulated a diminishing southward magnitude of extension concordant with the spreading rates extracted from the kinematic model of *Stamps et al.* [2014]. It has been shown that the width of rift basins positively correlates with colder and thicker lithosphere within various rift arms of the EARS [*Ebinger et al.*, 1999] as a consequence of larger effective elastic thicknesses representative of younger continental rift zones [*Petit and Ebinger*, 2000]. Heat flow estimates across the EARS also indicate that the lithospheric mantle beneath the western branch of the EARS is strong relative to the eastern branch [*Fadaie and Ranalli*, 1990], supporting the suggestion that the MRZ, which is the southernmost segment of the western branch, is situated in relatively strong lithosphere. Therefore, the existence of strong lithosphere may contribute to the delocalization of strain in the central MRZ.

4.3. Absence of Lower Mantle Influence on Rifting

The absence of MTZ thinning beneath the MRZ makes it unlikely that the present-day influence of hot mantle upwelling is a primary mechanism for extension. RF and tomographic analyses conducted by *Mulibo and Nyblade* [2013a, 2013b] suggested a broad lower mantle upwelling associated with the African superplume affecting a swath of thinned MTZ from beneath Zambia northward to northern Kenya and possibly the Afar Depression. Our observations are unable to support the existence of any low-velocity province beneath our study area residing above or within the MTZ, excepting a possible minor thermal anomaly beneath the NW

LRZ rift shoulder. Similarly, *Yu et al.* [2015a] found a thermally unperturbed MTZ beneath the ORZ and thus provided evidence for passive extension within the Okavango, probably driven by the antipolar rotation of the Congo and Kalahari cratonic blocks. Together with the apparently uplifted MTZ discontinuities detected by *Gao et al.* [2002] beneath the Kaapvaal craton of southern Africa, it is plausible that the existence of any low-velocity superplume-type structure is entirely confined to the lower mantle beneath southern Africa, favoring passive extension as the dominant mechanism for the initiation and development of rift zones situated therein.

Evidence supporting this hypothesis has been presented via various studies utilizing different techniques. Results produced from geodynamic modeling advocate divergence within the Nubia-Somalia plate system driven primarily, with little influence from convection-generated basal traction, by buoyancy within the African interior [*Stamps et al.*, 2015]. P_n and S_n tomography focused on the Tanzania Craton and the southern Tanganyika-Rukwa rift system revealed low uppermost-mantle temperatures, which suggest amagmatic extension within the southern western branch [*O'Donnell et al.*, 2016] absent the evidence of erosion of lithospheric mantle which is ubiquitous of mantle plume environments [*Davies*, 1994; *Rychert et al.*, 2012]. Recently developed kinematic models [e.g., *Saria et al.*, 2014; *Stamps et al.*, 2014] also demonstrate a clockwise-rotating Rovuma microplate (Figure 1a) with maximum Nubian relative velocities in the northern MRZ which diminish southward. This would imply that the MRZ is driven primarily by the plate-scale stress regime along the Nubia-Rovuma divergent boundary.

5. Conclusions

We present the first high-resolution imaging of the mantle transition zone discontinuities beneath the Malawi and Luangwa rift zones using newly acquired data consisting of 36 broadband seismic stations. Stacking of over 1900 individual RFs reveals a regional uplift of up to 20 km of both the *d*410 and *d*660 and regionally normal MTZ thicknesses. These findings imply not only the existence of high-velocity anomalies in the upper mantle, which we attribute to the existence of relatively thick lithosphere, but also the absence of a low-velocity province attributed to the African superplume within the upper mantle or MTZ beneath the study area. Minor thinning of the MTZ is observed parallel to the LRZ beneath its NW rift shoulder, which may be indicative of some influence of a thermal anomaly in the MTZ. Whether this anomaly is related to the recent reactivation of the LRZ remains as one of the unresolved problems in this poorly investigated section of the EARS. The thickening directly beneath and to the west of the MRZ could suggest a slightly hydrated MTZ. An E-W corridor of maximally thick lithosphere inferred in the study region striking orthogonally across the central MRZ could explain the formation of a wider rift basin bounded by immature border faults, as well as the southward diminishing of spreading rates. We postulate that, like the Okavango rift zone, the MRZ formed as the consequence of passive extensional processes probably associated with the rotation of the Rovuma microplate and its divergence from the Nubian plate. Finally, under the assumption that some of the mature segments of the EARS are subjected to active rifting, such as proposed by numerous studies [e.g., *Smith*, 1994; *Ritsema et al.*, 1999; *Huerta et al.*, 2009], the dominantly normal MTZ thickness beneath the young MRZ obtained from this study indicates that both active and passive rifting can coexist in a single rift system.

References

Ammon, C. J. (1991), The isolation of receiver effects from teleseismic *P*-waveforms, *Bull. Seismol. Soc. Am.*, *81*, 2504–2510.
Bagley, B., and A. A. Nyblade (2013), Seismic anisotropy in eastern Africa, mantle flow, and the African superplume, *Geophys. Res. Lett.*, *40*, 1500–1505, doi:10.1002/grl.50315.
Balmino, G., N. Vales, S. Bonvalot, and A. Briais (2012), Spherical harmonic modeling to ultra-high degree of Bouguer and isostatic anomalies, *J. Geod.*, *86*, 499–520, doi:10.1007/s00190-011-0533-4.
Banks, N. L., K. A. Bardwell, and S. Musiwa (1995), Karoo rift basins of the Luangwa Valley, Zambia, in *Hydrocarbon Habitat in Rift Basins*, edited by J. J. Lambiase, pp. 285–295, Geol. Soc. Spec. Publ., London, U. K.
Bastow, I. D., D. Keir, and E. Daly (2011), The Ethiopia Afar Geoscientific Lithospheric Experiment (EAGLE): Probing the transition from continental rifting to incipient seafloor spreading, in *Volcanism and Evolution of the African Lithosphere, Geol. Soc. Am. Spec. Pap.*, vol. 478, edited by L. Beccaluva, G. Bianchini, and M. Wilson, pp. 51–76, Geol. Soc. Am., Boulder, Colo., doi:10.1130/2011.2478(04).
Begg, G. C., et al. (2009), The lithospheric architecture of Africa: Seismic tomography, mantle petrology, and tectonic evolution, *Geosphere*, *5*, 23–50, doi:10.1130/GES00179.
Bina, C. R., and G. Helffrich (1994), Phase transition Clapeyron slopes and transition zone seismic discontinuity topography, *J. Geophys. Res.*, *99*, 15,853–15,860.
Bridges, D. L., K. Mickus, S. S. Gao, M. G. Abdelsalam, and A. Alemu (2012), Magnetic stripes of a transitional continental rift in Afar, *Geology*, *40*, 203–206, doi:10.1130/G32697.1.
Davies, G. F. (1994), Thermomechanical erosion of the lithosphere by mantle plumes, *J. Geophys. Res.*, *99*, 15,709–15,722, doi:10.1029/94JB00119.

Delvaux, D., K. Levi, R. Kajara, and J. Sorata (1992), Cenozoic paleostress and kinematic evolution of the Rukwa-North Malawi rift valley (East African Rift System), *Bull. Cent. Rech. Explor. Prod. Elf Aquitaine*, 16, 383–406.

Ebinger, C. J., B. R. Rosendahl, and D. J. Reynolds (1987), Tectonic model of the Malawi rift, Africa, *Tectonophysics*, 141, 215–235.

Ebinger, C. J., A. L. Deino, R. E. Drake, and A. L. Tesha (1989), Chronology of volcanism and rift basin propagation: Rungwe volcanic province, East Africa, *J. Geophys. Res.*, 94, 15,785–15,803.

Ebinger, C. J., J. A. Jackson, A. N. Foster, and N. J. Hayward (1999), Extensional basin geometry and the elastic lithosphere, *Philos. Trans. R. Soc. A*, 357, 741–765.

Efron, B., and R. Tibshirani (1986), Bootstrap methods for standard errors, confidence intervals, and other measures of statistical accuracy, *Stat. Sci.*, 1, 54–75.

Elsheikh, A. A., S. S. Gao, K. H. Liu, A. A. Mohamed, Y. Yu, and R. E. Fat-Helbary (2014), Seismic anisotropy and subduction-induced mantle fabrics beneath the Arabian and Nubian Plates adjacent to the Red Sea, *Geophys. Res. Lett.*, 41, 2376–2381, doi:10.1002/2014GL059536.

Fadaie, K., and G. Ranalli (1990), Rheology of the lithosphere in the East African Rift System, *Geophys. J. Int.*, 102, 445–453.

Fishwick, S. (2010), Surface wave tomography: Imaging of the lithosphere-asthenosphere boundary beneath central and southern Africa?, *Lithos*, 120, 63–73, doi:10.1016/j.lithos.2010.05.011.

French, S. W., and B. Romanowicz (2015), Broad plumes rooted at the base of the Earth's mantle beneath major hotspots, *Nature*, 525, 95–99, doi:10.1038/nature14876.

Fonseca, J. F. B. D., J. Chamussa, A. Domingues, G. Helffrich, E. Antunes, G. van Aswegen, L. V. Pinto, S. Custódio, and V. J. Manhiça (2014), MOZART: A seismological investigation of the East African Rift in central Mozambique, *Seismol. Res. Lett.*, 85, 108–116, doi:10.1785/0220130082.

Fritz, H., et al. (2013), Orogen styles in the East African Orogen: A review of the Neoproterozoic to Cambrian tectonic evolution, *J. Afr. Earth. Sci.*, 86, 65–106, doi:10.1016/j.jafrearsci.2013.06.004.

Gao, S. S., and K. H. Liu (2014a), Imaging mantle discontinuities using multiply-reflected *P*-to-*S* conversions, *Earth Planet. Sci. Lett.*, 402, 99–106, doi:10.1016/j.epsl.2013.08.025.

Gao, S. S., and K. H. Liu (2014b), Mantle transition zone discontinuities beneath the contiguous United States, *J. Geophys. Res. Solid Earth*, 119, 6452–6468, doi:10.1002/2014JB011253.

Gao, S. S., P. G. Silver, K. H. Liu, and the Kaapvaal Seismic Group (2002), Mantle discontinuities beneath southern Africa, *Geophys. Res. Lett.*, 29(10), 1491, doi:10.1029/2001GL013834.

Gao, S. S., et al. (2013), Seismic arrays to study African rift initiation, *Eos Trans. AGU*, 94, 213–214, doi:10.1002/2013EO240002.

Hansen, S. E., A. A. Nyblade, and M. H. Benoit (2012), Mantle structure beneath Africa and Arabia from adaptively parameterized *P*-wave tomography: Implications for the origin of Cenozoic Afro-Arabian tectonism, *Earth Planet. Sci. Lett.*, 319–320, 23–34, doi:10.1016/j.epsl.2011.12.023.

Helffrich, G. (2000), Topography of the transition zone seismic discontinuities, *Rev. Geophys.*, 38, 141–158.

Huerta, A. D., A. A. Nyblade, and A. M. Reusch (2009), Mantle transition zone structure beneath Kenya and Tanzania: More evidence for a deep-seated thermal upwelling in the mantle, *Geophys. J. Int.*, 177, 1249–1255, doi:10.1111/j.1365-246X.2009.04092.x.

Kennett, B. L. N., and E. R. Engdahl (1991), Traveltimes for global earthquake location and phase identification, *Geophys. J. Int.*, 105, 429–465.

Kuritani, T., E. Ohtani, and J.-I. Kimura (2011), Intensive hydration of the mantle transition zone beneath China caused by ancient slab stagnation, *Nat. Geosci.*, 4, 713–716, doi:10.1038/NGEO1250.

Laó-Dávila, D., H. S. Al-Salmi, M. G. Abdelsalam, and E. A. Atekwana (2015), Hierarchical segmentation of the Malawi rift: The influence of inherited lithospheric heterogeneity and kinematics in the evolution of continental rifts, *Tectonics*, 34, 2399–2417, doi:10.1002/2015TC003953.

Lemnifi, A. A., K. H. Liu, S. S. Gao, C. A. Reed, A. A. Elsheikh, Y. Yu, and A. A. Elmelade (2015), Azimuthal anisotropy beneath north central Africa from shear wave splitting analyses, *Geochem. Geophys. Geosyst.*, 16, 1105–1114, doi:10.1002/2014GC005706.

Leseane, K., E. A. Atekwana, K. L. Mickus, M. G. Abdelsalam, E. M. Shemang, and E. A. Atekwana (2015), Thermal perturbations beneath the incipient Okavango rift zone, northwest Botswana, *J. Geophys. Res. Solid Earth*, 120, 1210–1228, doi:10.1002/2014JB011029.

Litasov, K. D., E. Ohtani, A. Sano, A. Suzuki, and K. Funakoshi (2005), Wet subduction versus cold subduction, *Geophys. Res. Lett.*, 32, L13312, doi:10.1029/2005GL022921.

Liu, K. H., and S. S. Gao (2010), Spatial variations of crustal characteristics beneath the Hoggar swell, Algeria, revealed by systematic analyses of receiver functions from a single seismic station, *Geochem. Geophys. Geosyst.*, 11, Q08011, doi:10.1029/2010GC003091.

Liu, K. H., S. S. Gao, P. G. Silver, and Y. Zhang (2003), Mantle layering across central South America, *J. Geophys. Res.*, 108(B11), 2510, doi:10.1029/2002JB002208.

Mohamed, A. A., S. S. Gao, A. A. Elsheikh, K. H. Liu, Y. Yu, and R. E. Fat-Helbary (2014), Seismic imaging of mantle transition zone discontinuities beneath the northern Red Sea and adjacent areas, *Geophys. J. Int.*, 199, 648–657, doi:10.1093/gji/ggu284.

Molnar, P., P. C. England, and C. H. Jones (2015), Mantle dynamics, isostasy, and the support of high terrain, *J. Geophys. Res. Solid Earth*, 120, 1932–1957, doi:10.1002/2014JB011724.

Mulibo, G. D., and A. A. Nyblade (2013a), Mantle transition zone thinning beneath eastern Africa: Evidence for a whole-mantle superplume structure, *Geophys. Res. Lett.*, 40, 3562–3566, doi:10.1002/grl.50694.

Mulibo, G. D., and A. A. Nyblade (2013b), The *P* and *S* wave velocity structure of the mantle beneath eastern Africa and the African superplume anomaly, *Geochem. Geophys. Geosyst.*, 14, 2696–2715, doi:10.1002/ggge.20150.

Ni, S., D. V. Helmberger, and J. Tromp (2005), Three-dimensional structure of the African superplume from waveform modeling, *Geophys. J. Int.*, 161, 283–294, doi:10.1111/j.1365-246X.2005.02508.x.

O'Donnell, J. P., K. Selway, A. A. Nyblade, R. A. Brazier, N. El Tahir, and R. J. Durrheim (2016), Thick lithosphere, deep crustal earthquakes and no melt: A triple challenge to understanding extension in the western branch of the East African Rift, *Geophys. J. Int.*, 204, 985–998, doi:10.1093/gji/ggv492.

Ohtani, E., K. Litasov, T. Hosoya, T. Kubo, and T. Kondo (2004), Water transport into the deep mantle and formation of a hydrous transition zone, *Phys. Earth Planet. Inter.*, 143–144, 255–269, doi:10.1016/j.pepi.2003.09.015.

Owens, T. J., A. A. Nyblade, H. Gurrola, and C. A. Langston (2000), Mantle transition zone structure beneath Tanzania, East Africa, *Geophys. Res. Lett.*, 27, 827–830.

Petit, C., and C. Ebinger (2000), Flexure and mechanical behavior of cratonic lithosphere: Gravity models of the East Africa and Baikal rifts, *J. Geophys. Res.*, 105, 19,151–19,162.

Reed, C. A., S. Almadani, S. S. Gao, A. A. Elsheikh, S. Cherie, M. G. Abdelsalam, A. K. Thurmond, and K. H. Liu (2014), Receiver function constraints on crustal seismic velocities and partial melting beneath the Red Sea rift and adjacent regions, Afar Depression, *J. Geophys. Res. Solid Earth*, 119, 2138–2152, doi:10.1002/2013JB010719.

Reed, C. A., S. S. Gao, K. H. Liu, and Y. Yu (2016), The mantle transition zone beneath the Afar Depression and adjacent regions: Implications for mantle plumes and hydration, *Geophys. J. Int.*, *205*, 1756–1766, doi:10.1093/gji/ggw116.

Ringwood, A. E. (1975), *Composition and Petrology of the Earth's Mantle*, 1st ed., McGraw-Hill, 672 pp., New York.

Ringwood, A. E. (1991), Phase transformations and their bearing on the constitution and dynamics of the mantle, *Geochim. Cosmochim. Acta*, *55*, 2083–2110.

Ritsema, J., H. Jan van Heijst, and J. H. Woodhouse (1999), Complex shear wave velocity structure imaged beneath Africa and Iceland, *Science*, *286*, 1925–1928.

Rychert, C. A., et al. (2012), Volcanism in the Afar Rift sustained by decompression melting with minimal plume influence, *Nat. Geosci.*, *5*, 406–409, doi:10.1038/NGEO1455.

Saria, E., E. Calais, D. S. Stamps, D. Delvaux, and C. J. H. Hartnady (2014), Present-day kinematics of the East African Rift, *J. Geophys. Res. Solid Earth*, *119*, 3584–3600, doi:10.1002/2013JB010901.

Silver, P. G., S. S. Gao, K. H. Liu, and the Kaapvaal Seismic Group (2001), Mantle deformation beneath southern Africa, *Geophys. Res. Lett.*, *28*, 2493–2496.

Simmons, N. A., A. M. Forte, and S. P. Grand (2007), Thermochemical structure and dynamics of the African superplume, *Geophys. Res. Lett.*, *34*, L02301, doi:10.1029/2006GL028009.

Smith, M. (1994), Stratigraphic and structural constraints on mechanisms of active rifting in the Gregory Rift, Kenya, *Tectonophysics*, *236*, 3–22.

Smith, W. H. F., and P. Wessel (1990), Gridding with continuous curvature splines in tension, *Geophysics*, *55*, 293–305.

Stamps, D. S., L. M. Flesch, E. Calais, and A. Ghosh (2014), Current kinematics and dynamics of Africa and the East African Rift System, *J. Geophys. Res. Solid Earth*, *119*, 5161–5186, doi:10.1002/2013JB010717.

Stamps, D. S., G. Iaffaldano, and E. Calais (2015), Role of mantle flow in Nubia-Somalia plate divergence, *Geophys. Res. Lett.*, *42*, 290–296, doi:10.1002/2014GL062515.

Thompson, D. A., J. O. S. Hammond, J.-M. Kendall, G. W. Stuart, G. R. Helffrich, D. Keir, A. Ayele, and B. Goitom (2015), Hydrous upwelling across the mantle transition zone beneath the Afar Triple Junction, *Geochem. Geophys. Geosyst.*, *16*, 834–846, doi:10.1002/2014GC005648.

Yu, Y., K. H. Liu, M. Moidaki, C. A. Reed, and S. S. Gao (2015a), No thermal anomalies in the mantle transition zone beneath an incipient continental rift: Evidence from the first receiver function study across the Okavango rift zone, Botswana, *Geophys. J. Int.*, *202*, 1407–1418, doi:10.1093/gji/ggv229.

Yu, Y., S. S. Gao, M. Moidaki, C. A. Reed, and K. H. Liu (2015b), Seismic anisotropy beneath the incipient Okavango rift: Implications for rifting initiation, *Earth Planet. Sci. Lett.*, *430*, 1–8, doi:10.1016/j.epsl.2015.08.009.